Chapter 4

Emergence of a long-range ferroelectric order from a polar order at short ranges in a $K_{0.5}Na_{0.5}NbO_3$-based smart solution

4.1 Introduction

Physical properties of perovskite-based ferroelectric materials can be achieved by tuning inter-ferroelectric phase boundaries as a function of composition, temperature, pressure, etc. [53]. The temperature dependence (strong/weak) of inter-ferroelectric phase boundaries characterizes their type *viz.*, polymorphic phase boundary (PPB) or morphotropic phase boundary (MPB) [54, 57, 58]. The physical properties are known to enhance in the vicinity of PPB/MPB [54, 57, 58]. The enhancement of properties has been attributed to polarization rotation and/or polarization extension phenomena, and is linked with the flattening of the free energy profile [54, 57, 58]. Most of the MPBs are Pb-based *viz.*, $Pb(Ti_xZr_{1-x})O_3$ [53, 123], $Pb(Mg_{1/3}Nb_{2/3})O_3$-$PbTiO_3$ [124, 125], $Pb(Zn_{1/3}Nb_{2/3})O_3$-$PbTiO_3$ [46, 47], etc. Owing to the toxic effect of lead on human health and the environment, there is a surge in search for various Pb-free alternatives [48, 49].

Among various Pb-free alternatives, alkali niobates *viz.*, $LiNbO_3$, $NaNbO_3$, and $KNbO_3$ and their solid solutions *viz.*, $Li_xNa_{(1-x)}NbO_3$ (LNNx) and $K_xNa_{(1-x)}NbO_3$ (KNNx) have attracted considerable interest due to their high physical properties [111, 153, 161, 162, 166]. These high physical properties are due to inter-ferroelectric phase boundaries (PPB/MPB) exhibited by various alkali niobates and their solid solutions [54, 166]. For LNNx, a new MPB composition (x = 0.20; LNN20) has been identified using X-ray diffraction and PE loop data [166]. On the other hand, various reports exist for KNNx with an MPB at $x = 0.50$ (KNN50) [51, 53, 54, 153, 212]. Here, KNN50 is a solid solution of ferroelectric $KNbO_3$ having $Amm2$ ($1a_p \times \sqrt{2}b_p \times \sqrt{2}c_p$) space group and antiferroelectric $NaNbO_3$ having $Pbcm$ ($\sqrt{2}a_p \times \sqrt{2}b_p \times 4c_p$) space group. Orayech *et al.* investigated the temperature-dependent evolution of crystal structures for KNN50 using X-ray and neutron diffraction data [55]. Various crystal structures were found to follow the temperature sequence *viz.*, $R3c \xrightarrow{\approx 135K} Amm2 \xrightarrow{\approx 465K} P4mm \xrightarrow{\approx 700K} Pm\bar{3}m$ [55]. In an another study, Kong *et al.* analyzed temperature-dependent neutron diffraction data and found that the room temperature structure of KNN50 is monoclinic (Space Group: *Pm*), which is stable down to 100 K. They also demonstrated various ferrodistortive phase transitions at high temperatures *viz.*, $Pm \xrightarrow{\approx 471K} P4mm \xrightarrow{\approx 674K} Pm\bar{3}m$ [56]. Moreover, Kong *et al.*, Tripathi *et al.*, and Gupta *et al.* determined monoclinic structure (Space Group: *Pm*) stable also at short ranges for KNN50 using pair distribution function (PDF) data [56, 171, 212]. Further, Kong *et al.* demonstrated that KNN50 stabilizes into a completely ordered state at low temperatures with an order-disorder type transition at T $\approx$ 473 K [56].

Apart from alkali niobates, various alkaline earth metal-based perovskites *viz.*, $BaTiO_3$, $SrTiO_3$, $CaTiO_3$, etc., and their solid solutions are some of the Pb-free alternatives with numerous applications [24]. $BaTiO_3$ (BT) was the first perovskite material exhibiting ferroelectricity [153]. Moreover, the properties of BT can be tuned for various applications *via* doping at A and (or) B-sites [24, 153]. For instance, doping Strontium (Sr) at A-site of BT decreases the Curie temperature (T_C) [66]. On further increasing Sr content in BT, a relaxor ferroelectric like behavior has been observed. Among various Sr-doped compositions, $Ba_{0.9}Sr_{0.1}TiO_3$ (BST10) exhibits maximum dielectric response at ambient conditions [63, 64, 65, 66]. The sequence of temperature-dependent structural phase transitions of BST10 is analogous to pure BT ($R3m \xrightarrow{\approx 183K} Amm2 \xrightarrow{\approx 273K} P4mm \xrightarrow{\approx 393K} Pm\bar{3}m$ [12]) with a shift in T_C towards ambient temperature [63, 64, 65, 66].

The ferrodistortive phase transitions observed in KNN50 and BST10 are driven by the freezing of the phonon mode(s) corresponding to the Γ-point (q = 0,0,0) of the cubic Brillouin zone [24, 55, 236]. Among various phonon mode(s) associated with the Γ-point of cubic Brillouin zone, Γ_4^- phonon mode is three-dimensional triply degenerate and is responsible for ferroelectric displacements [24, 104]. Moreover, freezing of the Γ_4^- phonon mode results in the *P*4*mm*, *Amm*2, and *R*3*m* phases for order parameter directions (OPDs) *viz.*, (0,0,a), (a,a,0), and (a,a,a), respectively [24, 89]. Further, the monoclinic phase of KNN50 also results from the freezing of Γ_4^- phonon mode for (a,b,0) OPD [89]. Furthermore, the available ferroelectric content of the unit cell of a non-centrosymmetric crystal can be quantified using an ingenious method *viz.*, frozen phonon mode approach available at Bilbao Crystallographic Server [232, 233, 234, 235].

In the present work, we have synthesized a solid solution of KNN50 with BST10 *viz.*, (1-x)KNN50-xBST10 (*i.e.*, KBSTx for $0.00 \leq x \leq 0.20$) due to high dielectric response [63, 64, 65, 66] and morphotropic phase boundary (MPB) like behavior [51, 53, 153] of the parent materials *viz.*, BST10 and KNN50, respectively. We have analyzed the structure and properties of KBSTx ($0.00 \leq x \leq 0.20$) ceramics using X-ray diffraction, Raman scattering, and temperature-dependent dielectric data. Moreover, owing to MPB and order-disorder type behavior of KNN50 [56], we analyzed the temperature-dependent Synchrotron X-ray diffraction, Raman scattering, and pair distribution function data of KBST5. Further, we have used atomic coordinates, lattice parameters, Wyckoff site multiplicity, and polarization vectors to quantify the ferroelectric content available at long and short ranges as a function of composition and temperature using the frozen phonon mode approach [232, 233, 234, 235].

4.2 Experimental procedure

The (1-x)$K_{0.5}Na_{0.5}NbO_3$-$x$$Ba_{0.9}Sr_{0.1}TiO_3$ (KBSTx) ceramics for $0.00 \leq x \leq 0.20$ were synthesized *via* the solid-state reaction method using various precursors *viz.*, K_2CO_3 (Sisco Research Laboratories Pvt. Ltd.) (99%), Na_2CO_3 (HIMIDEA Labs) (99.5%), $BaCO_3$ (HIMIDEA Labs) (99%), $SrCO_3$ (HIMIDEA Labs) (99%), Nb_2O_5 (HIMIDEA Labs) (99.9%), and TiO_2 (HIMIDEA Labs) (99%), all of which were dried at 393 K before being weighed. The raw materials, once dried, were precisely weighed and then milled for a 24-hour period. Following the milling process, the milled powder was calcined at temperatures between 1123K and 1173K for a duration of 4 hours. After calcination, the powder was mixed with a 2-5% polyvinyl alcohol (PVA) binder and shaped into pellets under a pressure of 7-8 metric tons. These pellets were then sintered at temperatures ranging from 1323 K to 1388 K for 3-4 hours. The room temperature X-ray diffraction analysis was performed over the 2θ range of 20° to 120° with a step size of 0.02, using a Rigaku Miniflex 600 X-ray diffractometer with Cu-K_α radiation (Benchtop XRD). For dielectric measurements, electroding was done by applying silver paste to both sides of the sintered pellets. These measurements were conducted using a Keysight LCR meter in a frequency range from 1 kHz to 1 MHz and a temperature range from 100 K to 650 K.

The Raman scattering data of KBSTx ceramics for $0.00 \leq x \leq 0.20$ at ambient conditions were collected using the alpha300 RAS system from WITec with an excitation source of a 532 nm (green) laser. Moreover, the temperature-dependent Raman scattering data for 77 K $\leq T \leq$ 650 K were acquired using a Horiba LabRAM HR Raman spectrometer with an Olympus BX41 microscope attachment. An excitation wavelength of 514.5 nm from a Lexel Model-95 argon ion laser was used. The samples were placed in a Linkam THMS600 microscope stage for variable temperature Raman measurements. The laser beam was focused onto the sample using a 50x LWD objective (N.A.= 0.50), and the backscattered light was dispersed *via* a 600 lines/mm grating onto a liquid nitrogen cooled CCD detector. The data was acquired using LabSpec v5 software. Laser power at the sample was approximately 0.4 mW. This value was checked to verify that no local heating effects from the laser beam occurred.

The high-energy (λ = 0.1821Å) synchrotron X-ray diffraction data (SXRD) at elevated temperatures was obtained from Brookhaven National Lab for the temperature range 300 $\leq T \leq$ 1000 K. Moreover, the high-energy synchrotron data was used to obtain pair distribution function data. The first reduction step provided the structure function $S(Q)$ given as follows [208, 211]:

$$S(Q) = 1 + \frac{[I_{\text{coh}}(Q) - \Sigma c_i |f_i(Q)|^2]}{|\Sigma f_i(Q) c_i|^2} \tag{4.1}$$

Here, Q represents the wavevector ($Q = 4\pi \sin\theta/\lambda$) and 2θ is the angle between incident and scattered x-rays. $I_{\text{coh}}(Q)$ denotes the coherent portion of the diffraction data, while c_i and $f_i(Q)$ stand for the atomic concentrations and the x-ray structure factor of the i$^{\text{th}}$ atomic species, respectively. The structure factor, $S(Q)$, derived from high-energy synchrotron sources at Brookhaven National Lab, was measured over a wide Q range. To determine the final pair distribution function $G(r)$, the Fourier transform of $S(Q)$ was carried out with Q_{max}=18.1 Å^{-1} [208, 211]:

$$G(r) = \frac{2}{\pi} \int_{Q_{\text{min}}}^{Q_{\text{max}}} Q[S(Q) - 1] sin(Qr) dQ \tag{4.2}$$

Further, the frozen phonon modes decomposition has been analyzed utilizing the *AMPLIMODES* software [232, 233], which is accessible *via* the *Bilbao Crystallographic Server* [234, 235].

4.3 Result and discussion

4.3.1 X-ray diffraction analysis of KBSTx ceramics

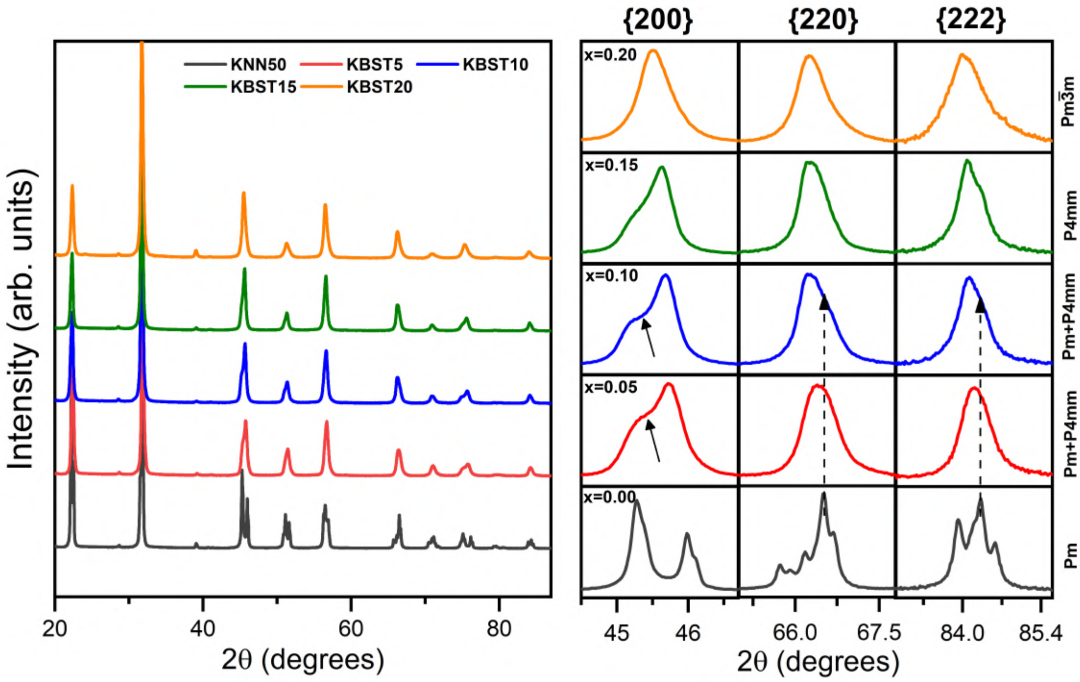

Fig. 4.1 X-ray diffraction patterns of KBSTx ceramics for $0.00 \leq x \leq 0.20$ and the evolution of the main perovskite peaks *viz.*, {200}, {220}, and {222} as a function of composition.

The average/long-range crystal structure of KBSTx ceramics for $0.00 \leq x \leq 0.20$ is determined using X-ray diffraction data. The solid solution is formed with a trace amount ($< 1\%$) of the secondary phase *i.e.*, $Na_{13}Nb_{35}O_{94}$ (Space Group: *Pba*2) [255] (see Fig. 4.1). Figure 4.1 depicts the evolution of main perovskite peaks *viz.*, {200}, {220}, and {222} as a function of composition. For $x = 0.00$ (KNN50), the splitting of the main perovskite peaks suggests a monoclinic phase. For $x = 0.05$ (KBST5), the changes in the peak shape suggest a tetragonal symmetry with additional features corresponding to the monoclinic phase of KNN50 (see black arrows in Fig. 4.1). Moreover, for $x = 0.10$ (KBST10), the peak profiles are analogous to KBST5, suggesting two-phase coexistence. For $x = 0.15$ (KBST15), the peak profiles suggest a single tetragonal phase and for $x = 0.20$ (KBST20), all the peaks exhibit a singlet nature, suggesting cubic symmetry. However, a broadening in the tail of the main perovskite peaks can be observed for KBST20, suggesting the presence of disorder in the material [7], which will be quantified using temperature-dependent dielectric data in the upcoming section.

Further, the above-suggested crystal structures are confirmed *via* Rietveld analysis using FULLPROF program [239]. The initial structural parameters for the monoclinic phase were taken from the literature [56]. For $x = 0.00$, the monoclinic model with Pm space group provides satisfactory fit (see Fig. 4.2(a)). The insets in Fig. 4.2 represent the zoomed view of profile fitting for main perovskite peaks. For KBST5, we first used a single tetragonal model with a $P4mm$ space group where misfits were observed for (200) and (222) peaks (see black arrows in the insets of Fig. 4.2(b)). As discussed earlier, we used another phase corresponding to the crystal structure *viz.*, monoclinic (Space Group: Pm) of one of the parent (KNN50) at ambient conditions. The two-phase refinement using tetragonal (Space Group: $P4mm$) and monoclinic (Space Group: Pm) structure fits the XRD pattern satisfactorily (see Fig. 4.2(b)) with good agreement factors. This exercise confirms the two-phase model for KBST5 and KBST10 (see Fig. 4.2(c)). On further increasing BST10 content, a single tetragonal phase (Space Group: $P4mm$) fits the XRD pattern of KBST15 very well (see Fig. 4.2(d)). Furthermore, for KBST20 the disordered cubic phase with $Pm\bar{3}m$ space group has been confirmed using Le Bail refinement (see Fig. 4.2(e)) [7]. Various structural phase transitions observed as a function of composition are summarized in Table 4.1. The structural parameters, along with the agreement factors, are mentioned in the tables below (see Tables 4.2, 4.3, 4.4, and 4.5). Further, increase in disorder with increasing BST10 content has been analyzed using temperature-dependent dielectric data in the next section.

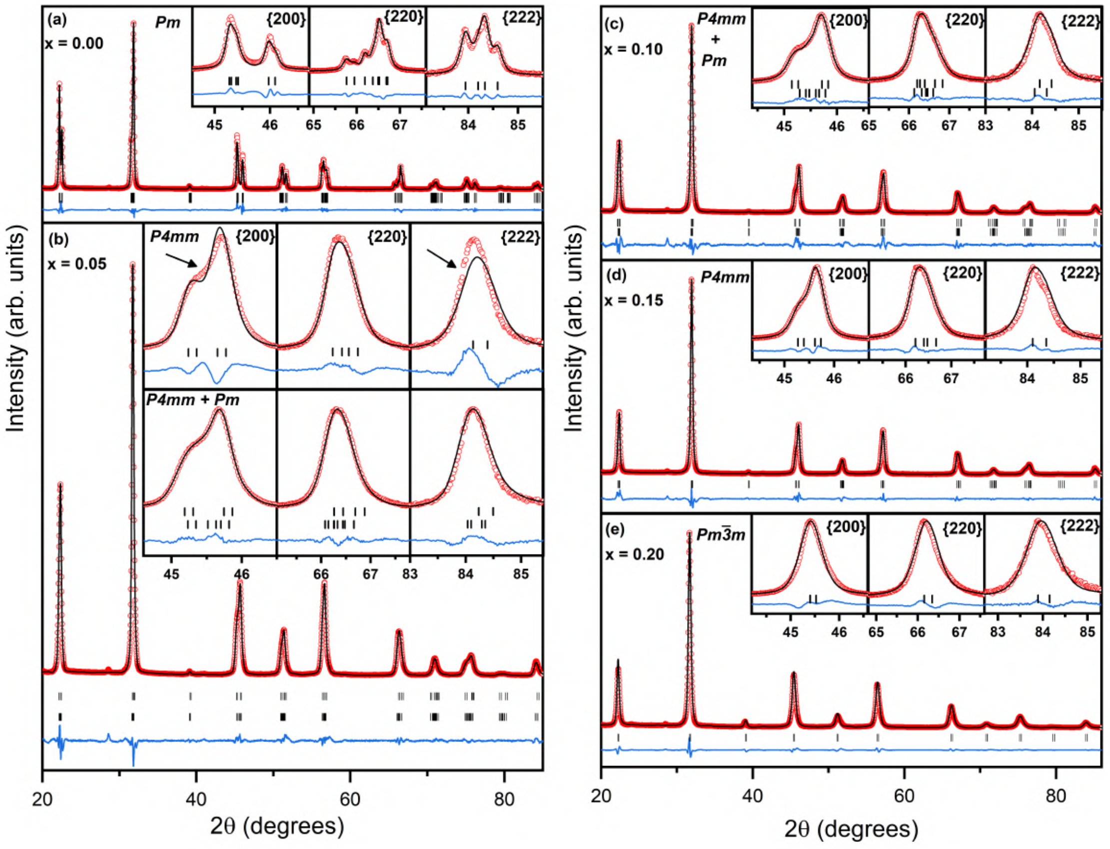

Fig. 4.2 The XRD profiles of KBST*x* ceramics at ambient conditions fitted using Rietveld analysis. Different models have been used for fitting *viz*., *Pm* model for $x = 0.00$, (*Pm* + *P*4*mm*) model for $x = 0.05$ and 0.10, and *P*4*mm* model for $x = 0.15$. Moreover, a cubic symmetry (Space Group: $Pm\bar{3}m$) is used to fit the XRD profile for $x = 0.20$ using the Lebail method (Tripathi *et al*., 2024) [7]. The open red circles represent the observed diffraction pattern, the black continuous line represents the calculated profile, and the blue line represents the difference between the observed and calculated patterns.

Table 4.1 Various structural phase transitions in KBST*x* ceramics.

BST content (*x*)	Structure (Sapce Group)
0.00 (KNN50)	Monoclinic (*Pm*)
0.05 (KBST5)	Monoclinic (*Pm*) + Tetragonal (*P*4*mm*)
0.10 (KBST10)	Monoclinic (*Pm*) + Tetragonal (*P*4*mm*)
0.15 (KBST15)	Tetragonal (*P*4*mm*)
0.20 (KBST20)	Cubic ($Pm\bar{3}m$)

Table 4.2 Various structural parameters, and agreement factors obtained from the Rietveld refinements of the X-ray diffraction patterns (at ambient conditions) for x = 0.00 (KNN50) using the *Pm* model.

Rietveld Refinement				
Space group: *Pm*				
Atoms	x	y	z	B_{iso}(Å^2)
K/Na	0.0535(15)	0.0000	0.0441(7)	0.332(37)
Nb	0.5529(10)	0.5000	0.5871(7)	0.508(16)
O_1	0.5806(41)	0.0000	0.5353(38)	0.239(137)
O_2	0.0544(84)	0.5000	0.5798(60)	1.284(142)
O_3	0.6024(24)	0.5000	0.0691(31)	0.101(136)
a=4.000(1)Å, b=3.945(1)Å, c=4.003(1)Å, β=90.330(2)				
V=63.173(2)Å^3				
Agreement factors: R_p = 3.87, R_{wp} = 5.68, R_{exp} = 2.93, χ^2 = 3.76				

Table 4.3 Various structural parameters, and agreement factors obtained from the Rietveld refinements of the X-ray diffraction patterns (at ambient conditions) for x = 0.05 (KBST5) using (*Pm* + *P*4*mm*) model.

Rietveld Refinement								
	Space group: *Pm*				Space group: *P*4*mm*			
Atoms	x	y	z	B_{iso}(Å^2)	x	y	z	B_{iso}(Å^2)
K/Na/Ba/Sr	0.0032(9)	0.0000	0.0158(8)	0.314(19)	0.0000	0.0000	0.0037(15)	0.810(34)
Nb/Ti	0.5215(9)	0.5000	0.5363(52)	0.336(9)	0.5000	0.5000	0.4825(12)	0.278(14)
O_1	0.5407(42)	0.0000	0.5024(21)	0.035(91)	0.5000	0.5000	0.0449(31)	0.434(274)
O_2	0.0226(100)	0.5000	0.4923(22)	0.991(125)	0.5000	0.0000	0.4766(35)	0.042(93)
O_3	0.5479(36)	0.5000	0.0387(35)	0.569(92)				
	a=3.982(1)Å, b=3.967(1)Å, c=4.006(1)Å, β=90.051(6)				a=3.963(1)Å, c=4.009(1)Å			
	V=63.297(2)Å^3				V=62.980(5)Å^3			
	Phase fraction = 57.67% (0.73)				Phase fraction = 42.33% (0.64)			
Agreement factors: R_p=2.13, R_{wp}=2.97, R_{exp}=1.58, χ^2=3.51								

Table 4.4 Various structural parameters, and agreement factors obtained from the Rietveld refinements of the X-ray diffraction patterns (at ambient conditions) for x = 0.10 (KBST10) using (*Pm* + *P*4*mm*) model.

Rietveld Refinement								
	Space group: *Pm*				Space group: *P*4*mm*			
Atoms	x	y	z	B_{iso}(Å^2)	x	y	z	B_{iso}(Å^2)
K/Na/Ba/Sr	0.0050(40)	0.0000	0.0044(20)	0.295(36)	0.0000	0.0000	0.0014(96)	1.054(18)
Nb/Ti	0.5007(19)	0.5000	0.5224(21)	0.667(23)	0.5000	0.5000	0.4880(6)	0.478(9)
O_1	0.5221(83)	0.0000	0.4743(56)	0.539(230)	0.5000	0.5000	0.0572(15)	0.172(166)
O_2	0.0264(64)	0.5000	0.6031(45)	0.939(292)	0.5000	0.0000	0.5009(15)	0.167(63)
O_3	0.5321(70)	0.5000	0.0248(195)	1.217(262)				
	a=3.984(1)Å, b=3.968(1)Å, c=4.004(1)Å, β=89.982(78)				a=3.965(1)Å, c=4.0091(2)Å			
	V=63.323(4)Å^3				V=63.058(3)Å^3			
	Phase fraction = 22.04% (0.34)				Phase fraction = 77.96% (0.53)			
Agreement factors: R_p=2.22, R_{wp}=2.92, R_{exp}=1.53, χ^2=3.64								

4.3.2 Dielectric analysis of KBST*x* ceramics

The temperature-dependent dielectric data has been collected for KBST*x* ceramics (0.00 $\leq x \leq$ 0.20) for a wide temperature range (105 K $\leq T \leq$ 650 K). Figure 4.3 depicts the

Table 4.5 Various structural parameters, and agreement factors obtained from the Rietveld refinements of the X-ray diffraction patterns (at ambient conditions) for $x = 0.15$ (KBST15) using *P*4*mm* model.

Rietveld Refinement				
Space group: *P*4*mm*				
Atoms	x	y	z	$B_{\text{iso}}(\text{Å}^2)$
K/Na/Ba/Sr	0.0000	0.0000	0.0005(8)	0.956(17)
Nb/Ti	0.5000	0.5000	0.4827(4)	0.529(7)
O_1	0.5000	0.5000	0.0268(16)	0.498(92)
O_2	0.5000	0.0000	0.5127(11)	0.314(43)
a=3.974(1)Å, c=4.0028(1)Å				
V=63.234(1)Å^3				
Agreement factors: $R_p = 2.76$, $R_{wp} = 3.61$, $R_{exp} = 1.56$, $\chi^2 = 5.36$				

Table 4.6 Various temperatures corresponding to the real part of the dielectric constant of KBSTx ceramics. Here, T_C is the Curie temperature for normal ferroelectrics (for $0.00 \leq x \leq 0.15$), and T_m is the temperature corresponding to dielectric maxima observed for ceramics exhibiting diffuse phase transitions ($x = 0.20$). Note: The temperatures corresponding to KNN50 ceramics have been taken from the literature (Kong *et al.*, 2021).

Composition	$T_{\text{M-T}}$ (K)	T_C/T_m (K)	T_B (K)	ΔT_m (K)
KNN50	471	674	-	-
KBST5	297	551	565	14
KBST10	293	497	542	45
KBST15	-	460	511	51
KBST20	-	323	388	65

real (ε') and imaginary (ε'') part of the dielectric constant for KBSTx at 100 kHz. For KNN50, structural phase transition temperatures *viz.*, monoclinic to tetragonal ($T_{\text{M-T}}$), and tetragonal to cubic (T_C) are reported as 471 K, and 674 K [56], respectively. The above-mentioned dielectric anomalies shift to lower temperatures with increasing BST10 content in KNN50, *i.e.*, for KBST5 and KBST10. Specifically, $T_{\text{M-T}}$ and T_C shifts at lower temperatures *viz.*, 297 K and 551 K for KBST5, and 293 K and 497 K for KBST10 ceramics (see Figs. 4.3(a)-(b)). Moreover, a broad and diffuse dielectric peak is observed for KBST15 and KBST20 with a maximum around 460 K, and 323 K, respectively (see Figs. 4.3(c)-(d)). The long-range crystal structure of KBST15 is tetragonal (see Fig. 4.2(d)) with a dielectric peak at T $\approx$ 460 K corresponding to the ferroelectric (Space Group: *P*4*mm*)-paraelectric (Space Group: $Pm\bar{3}m$) phase transition (see Fig. 4.3(c)). Further, KBST20 exhibits a disordered cubic structure at long ranges having dielectric

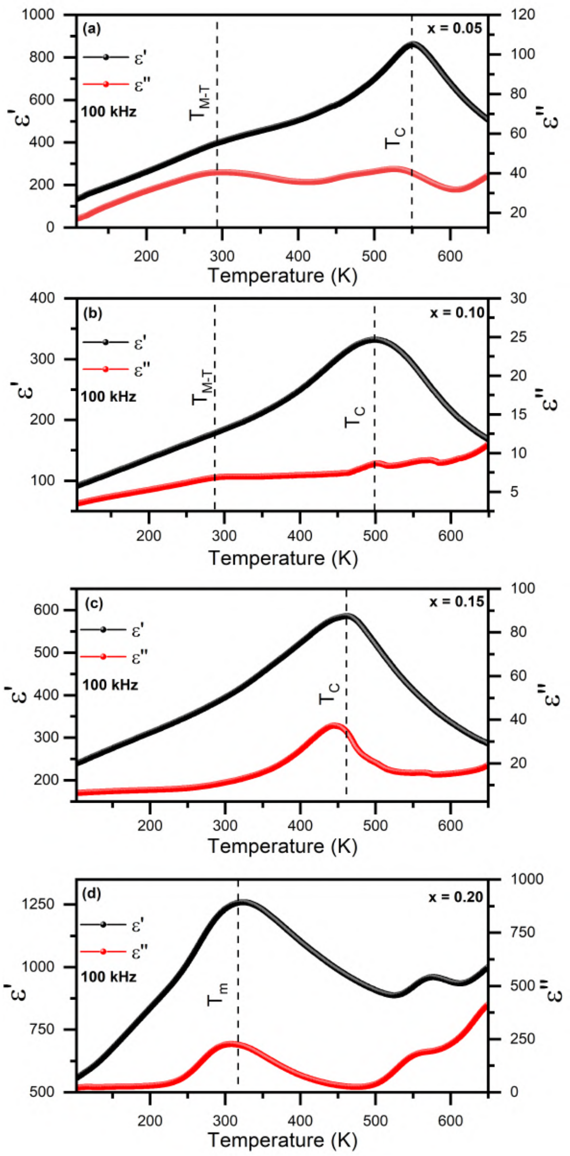

Fig. 4.3 The plot between real (ε') and imaginary (ε'') part of dielectric constant of KBSTx ceramics. Here, $T_{M\text{-}T}$, T_m, and T_C represent the temperature corresponding to the monoclinic to tetragonal phase transition, the temperature corresponding to the dielectric maxima, and the Curie temperature, respectively.

maxima at $T \approx 323$ K (see Fig. 4.3(d)) [7]. The dielectric behavior of normal ferroelectric materials follow Curie-Weiss law above Curie temperature (T_C) [22, 256, 257]. However, for disordered materials with diffused dielectric peaks, the dielectric behavior deviates from the Curie-Weiss law below a certain temperature, referred as Burns temperature (T_B)

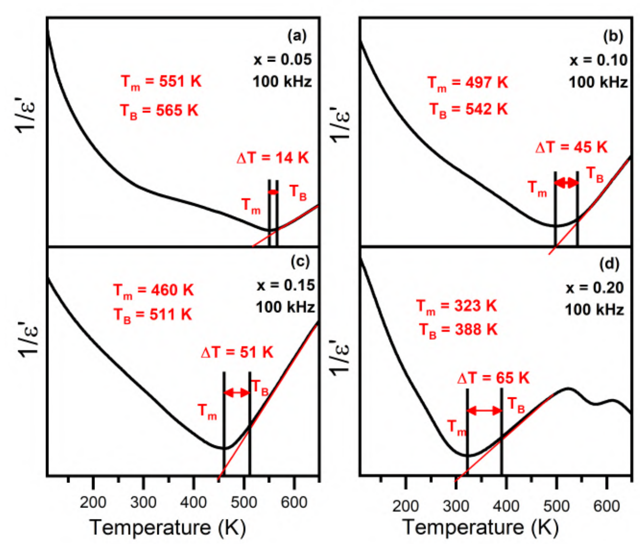

Fig. 4.4 The plot between the inverse of the real part of the dielectric constant (ε') and temperature (T) for KBSTx ceramics.

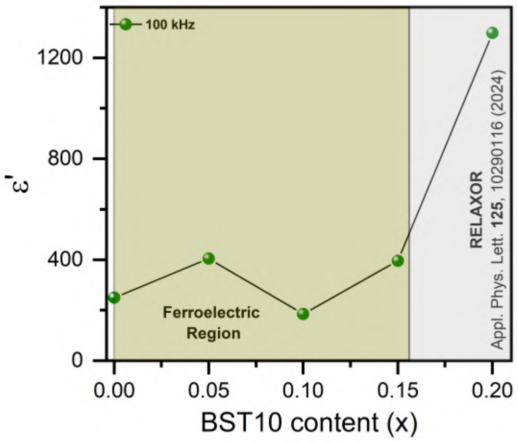

Fig. 4.5 Evolution of room temperature dielectric constant at 100 kHz for KBSTx ceramics.

[5, 22]. The deviation from Curie-Weiss law is linked to an increase in diffuseness of the dielectric peak and is quantified by the following relation [22, 256]:

$$\Delta T_{\mathrm{m}} = T_{\mathrm{B}} - T_{\mathrm{m}} \tag{4.3}$$

Here, $\Delta \mathrm{T_m}$ quantifies the relative diffuseness of the dielectric peak originating from an increase of disorder in the material. Figure 4.4 depicts the plot between the inverse of the real part of the dielectric constant and temperature, for different compositions. With increasing BST10 content (x), ΔT_m increases and attains a maximum value at KBST20 (see Fig. 4.4 and Table 4.6). This results due to increase in mismatch of ionic radii/oxidation states of the dopants at A/B site [7, 118]. Further, the room temperature dielectric constant exhibits a maximum at KBST5 in the ferroelectric region (see Fig. 4.5). Specifically, the dielectric constant for KBST5 is more than its adjacent compositions *viz.*, KNN50 and KBST10 by $\approx$ 62 % and 83 %, respectively. High dielectric maxima for KBST5 is reminiscent of an MPB-like behavior [111], and is closely linked with the coexistence of two ferroic phases. The increase in dielectric constant for $x > 0.15$ is due to the transition from ferroelectric region into a relaxor ferroelectric region [7]. The relaxor nature of KBST20 will be discussed in the next chapter. Further, the MPB-like behavior of KBST5 has been analyzed for its temperature-dependent behavior in the upcoming section.

4.3.3 SXRD analysis of KBST5 ceramics at elevated temperatures

The room temperature dielectric maxima of KBST5 at ambient conditions has been attributed to the MPB-like behavior [111], where the two ferroelectric phases *viz.*, tetragonal (Space Group: *P*4*mm*) and monoclinic (Space Group: *Pm*) co-exist. Moreover, to explore the structure of KBST5 as a function of temperature, we have obtained synchrotron X-ray diffraction (SXRD) data for a wide temperature range (300 K $\leq T \leq$ 1000 K). Figure 4.6 depicts the evolution of main perovskite peaks *viz.*, {200}, {220}, and {222} as a function of temperature. The SXRD analysis confirms the co-existence of two phases at ambient conditions as inferred from Benchtop XRD (see black arrow in Fig. 4.6). The two ferroelectric phases are stable for $T < 400$ K. Moreover, a single tetragonal and a single cubic phases are stable for 400 K $\leq T \leq$ 500 K and 550 K $\leq T \leq$1000 K, respectively. These crystal structures of KBST5 have been confirmed *via* Rietveld analysis using the FULLPROF program [239]. The starting structural parameters for Rietveld refinements of

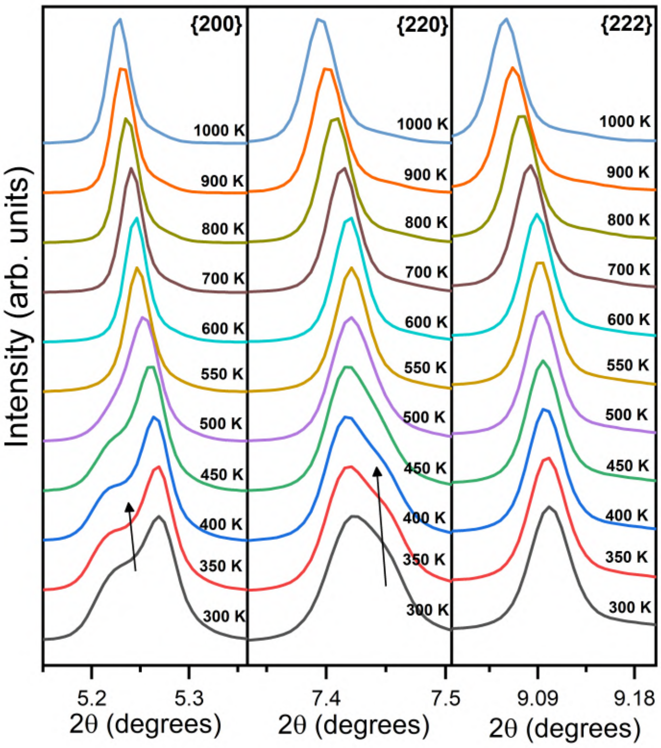

Fig. 4.6 Evolution of main perovskite peaks as a function of temperature (300 K $\leq T \leq$ 1000 K) of KBST5 ceramics.

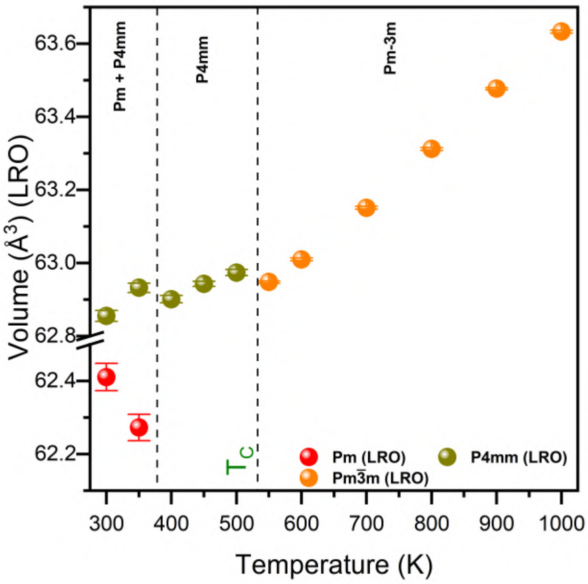

Fig. 4.7 Evolution of volume (at long ranges) of KBST5 ceramics as a function of temperature.

the SXRD data were taken from the room temperature refinement of the benchtop XRD data. Figure 4.7 depicts the volume of KBST5 as a function of temperature obtained after Rietveld refinements of SXRD data. The volume increases with increasing temperature (see Fig. 4.7), with two anomalies at $\mathrm{T} \approx 400$ K and 550 K. The anomaly around 400 K corresponds to the disappearance of the monoclinic phase, and the anomaly around 550 K corresponds to the ferroelectric (Space Group: $P4mm$) $\rightarrow$ paraelectric (Space Group: $Pm\bar{3}m$) transition. Thus, we observe that the two ferroelectric phases (Pm+$P4mm$) of KBST5 are stable for $T < 400$ K, suggesting a weak temperature dependence which is a characteristic feature of an MPB. Further, the ferroelectric content of various polar/non-centro symmetric phases is quantified using the frozen phonon mode approach, which is discussed in the upcoming section.

4.3.4 Frozen phonon mode approach

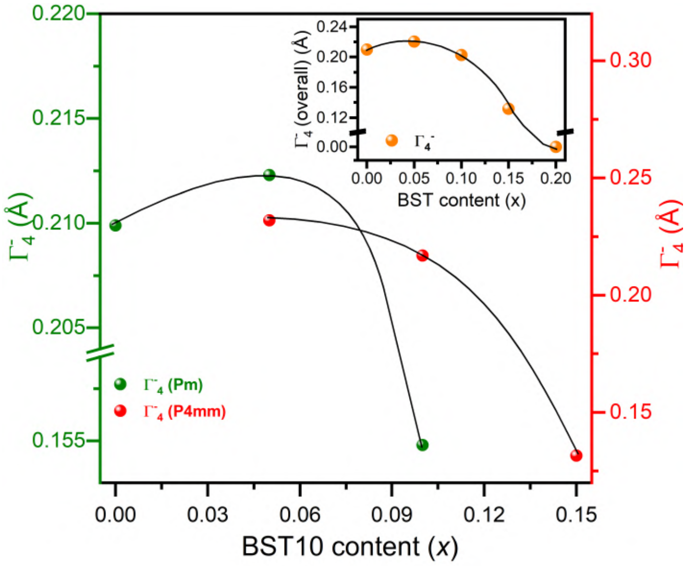

Fig. 4.8 Evolution of the amplitude of ferroelectric phonon mode (Γ_4^-) with compositions (x). The top right inset represents the evolution of the overall amplitude of Γ_4^- phonon mode as a function of compositions (x). Here, the amplitude of the Γ_4^- phonon mode has been calculated using the structural parameters obtained after Rietveld analysis of benchtop XRD data of KBSTx ceramics.

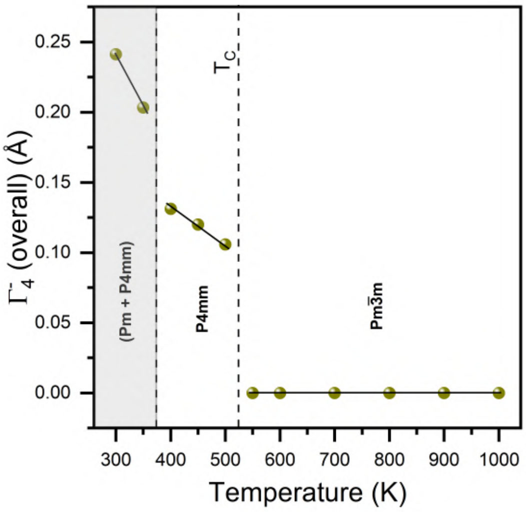

Fig. 4.9 Evolution of the overall amplitude of Γ_4^- phonon mode of KBST5 as a function of temperature. Here, the amplitude of the Γ_4^- phonon mode has been calculated using the structural parameters obtained after Rietveld analysis of temperature-dependent SXRD data of KBST5 ceramics.

Various composition and temperature-dependent ferrodistortive phase transitions observed in KBST*x* ceramics are driven by the freezing of soft phonon modes associated with the zone center of the cubic Brillouin zone [24]. The static atomic displacements responsible for low symmetry phases are quantified in terms of the amplitudes of the frozen phonon modes [24, 232, 252, 253]. The low symmetry ferroelectric phases *viz.*, *P*4*mm*, *Amm*2, *R*3*m*, and *Pm* result from the component freezing of Γ_4^- phonon mode (associated with Γ-point *i.e.*, $q = (0,0,0)$ of the cubic Brillouin zone) with various order parameter directions (OPDs) [24, 89]. The low symmetry phase is related to the high symmetry cubic phase by the following relation [236]:

$$r(\mu,i) = r_0(\mu,i) + u(\mu,i) \tag{4.4}$$

where r(μ, i) corresponds to the position of the μ^{th} (= 1, 2, 3, 4,....) atom of low symmetry space group, $r_0(\mu$, i) corresponds to the atomic positions of the high symmetry space group and u(μ, i) corresponds to the static displacements included in the low symmetry phase.

Moreover, a cubic phase ($Pm\bar{3}m$ space group) with lattice parameter a = 3.99171 Å, A-site, B- site, and Oxygen atoms with Wyckoff positions *viz.*, 1b (0.5,0.5,0.5), 1a (0,0,0), and 3d (0.5,0,0) are used as a reference structure for the calculation of the amplitude of the frozen phonon mode(s).

The low symmetry monoclinic and tetragonal phase confirmed for KBST*x* ceramics result from the freezing of Γ_4^- phonon mode with (a,b,0) and (0,0,a) order parameter directions, respectively [258]. Here, Γ_4^- phonon mode is referred to as primary phonon mode as it is responsible for symmetry breaking [191]. The amplitude of Γ_4^- phonon mode is a measure of ferroelectric polarization of the unit cell. Figure 4.8 depicts the evolution of the amplitude of Γ_4^- phonon mode as the function of composition. The amplitude of Γ_4^- phonon mode corresponding to monoclinic phase first increases for x = 0.05 (KBST5), and then decreases for $x > 0.05$ (see Fig. 4.8). This corroborates the conclusions inferred from the composition-dependent dielectric data. The overall mode amplitude for the two-phase region has been calculated using phase fractions. Further, this overall amplitude also maximizes at KBST5, supplementing MPB-like behavior.

Furthermore, we have also calculated the amplitude of the Γ_4^- phonon mode as a function of temperature for KBST5. Figure 4.9 depicts the overall amplitude of Γ_4^- phonon mode with temperatures. The amplitude decreases as the temperature increases, with two anomalies at T $\approx$ 400 K and 550 K corresponding to the phase transitions *viz.*, (Pm+$P4mm$) $\xrightarrow{\approx 400K} P4mm \xrightarrow{\approx 550K} Pm\bar{3}m$ inferred from temperature-dependent SXRD and dielectric data.

4.3.5 Raman study of KBST*x* ceramics

Ferrodistortive phase transitions (q = 0,0,0) in ferroelectric materials can be characterized by Raman active modes [21]. The appearance/disappearance of various Raman active modes are indicators of structural phase transitions [21]. Raman spectroscopic technique

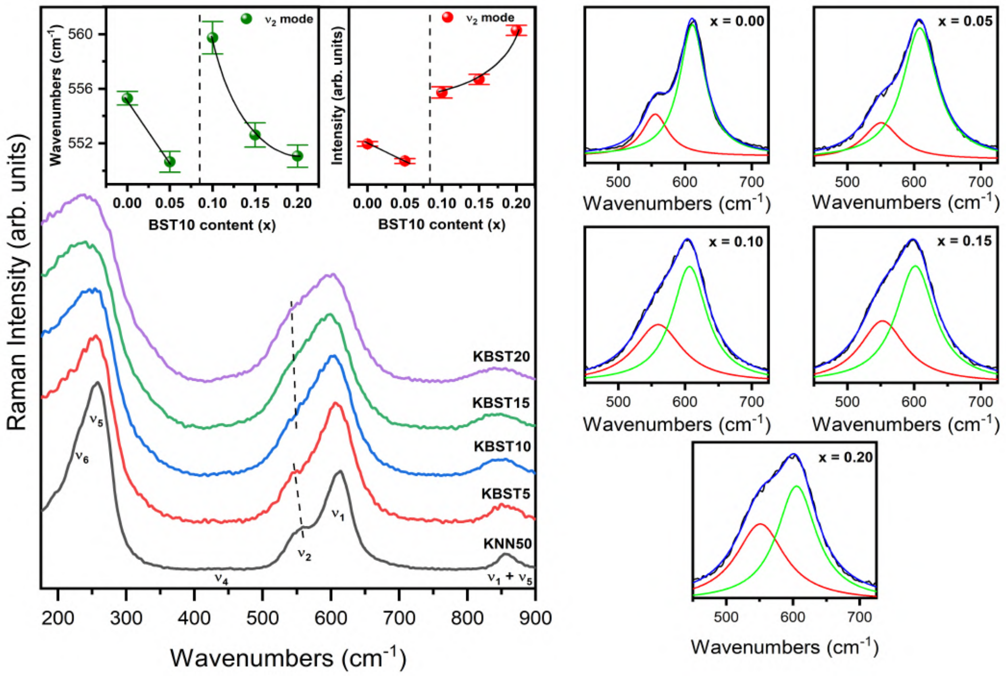

Fig. 4.10 The Raman spectra of KBST*x* ceramics. The top left and top right inset represent the variation of wavenumber and intensity of ν_2 mode with compositions. The figures on the right represent the fitting of the prominent Raman peak (500 cm^{-1}-700 cm^{-1}) using the Lorentz function for KBST*x* ceramics.

is sensitive to internal vibrations of BO_6 octahedra, which cannot be probed using conventional X-ray diffraction technique [21, 202]. For instance, Pb(Mg,Nb)O_3 (PMN) is a well-known relaxor ferroelectric exhibiting an average cubic structure at long ranges which is determined by using X-ray diffraction data [242, 259, 260] whereas, Raman analysis uncovers the symmetry of polar nanoregions (rhombohedral) at short ranges [141, 261], which can not be probed by using X-ray diffraction data. Thus, overall structure of PMN at various length scales (long and short ranges) has been determined by analyzing X-ray diffraction and Raman scattering data [202]. Most of the perovskite-based ferroelectric materials are known to stabilize in paraelectric cubic phase (Space Group: $Pm\bar{3}m$) at high temperatures [24, 262]. In the cubic phase (Space Group: $Pm\bar{3}m$), there are five triply degenerate phonon modes *i.e.*, a total of 15 phonon modes associated with the five atoms of ABO_3 (three acoustic and twelve optical phonon modes) [262]. All the phonon modes

Table 4.7 Description of various irreps corresponding to the cubic and monoclinic phase with $Pm\bar{3}m$, $P4mm$, and Pm space groups, respectively.

	Space Group: $Pm\bar{3}m$	
Atom	Wyckoff site	Irrep(s)
A	1b	T_{1u}
B	1a	T_{1u}
O	3d	$T_{2u} + 2T_{1u}$
	$\Gamma_{total} = 4T_{1u}+T_{2u}$ $\Gamma_{acoustic} = T_{1u}$ $\Gamma_{optical} = 3T_{1u}+T_{2u}$	
	Space Group: $P4mm$	
Atom	Wyckoff site	Irrep(s)
A	1a	$A_1 + E$
B	1b	$A_1 + E$
O1	1b	$A_1 + E$
O2	2c	$(A_1 + E) + (B_1 + E)$
	$\Gamma_{total} = 4A_1 + B_1 + 5E$ $\Gamma_{acoustic} = A_1 + E$ $\Gamma_{optical} = 3A_1 + B_1 + 4E$	
	Space Group: Pm	
Atom	Wyckoff site	Irrep(s)
A	1a	$2A' + A''$
B	1b	$2A' + A''$
O1	1b	$2A' + A''$
O2	1b	$2A' + A''$
O3	1a	$2A' + A''$
	$\Gamma_{total} = 10A' + 5A''$ $\Gamma_{acoustic} = 2A' + A''$ $\Gamma_{optical} = 8A' + 4A''$	

associated with the cubic phase are Raman inactive (*i.e.*, no Raman peaks are detected for cubic symmetry) [262]. Each atom at a specific Wyckoff site corresponds to phonon mode(s) mentioned in Table 4.7. The five triply degenerate phonon modes of $Pm\bar{3}m$ space group *viz.*, $4T_{1u}$ and T_{2u} correspond to A site, B site, and oxygen atoms placed at 1b, 1a, and 3d Wyckoff sites, respectively. These triply degenerate phonon modes split into three one-dimensional phonon modes *viz.*, 2A'+A" (associated with unique atomic positions in low symmetry space group) in the monoclinic symmetry with the *Pm* space group (see Table 4.7).

Figure 4.10 depicts the evolution of Raman spectra as a function of composition. The Raman spectrum of $x = 0.00$ (KNN50) reveals monoclinic structure similar to what has been reported for KNN50 [7, 168, 212, 241]. On the other hand, monoclinic structure has been reported at short ranges for $x = 0.20$ (KBST20) using temperature-dependent Raman scattering data [7]. The prominent Raman peaks near 610 cm^{-1} (ν_1), 550 cm^{-1} (ν_2), 450 cm^{-1} (ν_4), 270 cm^{-1} (ν_5), 230 cm^{-1} (ν_6), and 850 cm^{-1} (ν_1+ν_5) are observed for all the compositions, suggesting monoclinic distortions for KBSTx ceramics. The presence of (ν_1+ν_5) peak for all the compositions ($0.00 \leq x \leq 0.20$) depicts polar distortions in the unit cell [7]. The long and short-range symmetry of KNN50 is monoclinic, confirming earlier conclusions from X-ray diffraction, Raman scattering, and PDF studies [56, 171, 212], inferring an ordered state. As discussed earlier, the disorder in KBSTx ceramics increases with the increase in BST10 content; for KBST5 and KBST10, we observe two co-existing ferroelectric phases (*viz.*, monoclinic and tetragonal) at long ranges whereas monoclinic phase at short ranges. Therefore, a disordered state is concluded (for KBST5 and KBST10) from the combined analysis of X-ray diffraction and Raman scattering data. Moreover, for KBST15 and KBST20, a tetragonal and a cubic phase are found to be stable at long ranges, respectively, whereas a monoclinic phase is stable at short ranges, suggesting a disordered state in the material [7]. Thereafter, a transition from an ordered state to a disordered state is concluded from the combined analysis of X-ray diffraction and Raman scattering data, confirming the emergence of long-range ferroelectric order (observed for KNN50) from a short-range polar order with monoclinic symmetry (observed for KBST20). Moreover, the evolution of wavenumbers and intensity of one of the prominent Raman peaks (*i.e.*, ν_2 mode) has been analyzed as a function of composition (see the inset of Fig.

4.10). A clear anomaly near $x = 0.10$ (KBST10) is observed in wavenumber and intensity. This anomaly has been attributed to the transition of a monoclinic phase in an ordered state (here monoclinic phase dominates at long ranges for $x < 0.10$ with a monoclinic phase stable at short ranges too) into the monoclinic phase of the disordered state (here a tetragonal phase dominates for $x = 0.10$ and then a cubic phase is stable for $x = 0.20$ at long ranges, with a monoclinic phase stable at short ranges). Here, it is important to note that the monoclinic symmetry concluded from Raman data of KNN50 corresponds to both long- and short ranges [56, 168, 171, 241], whereas polar monoclinic symmetry concluded from Raman data of KBST20 corresponds only to short ranges contrary to a non-polar cubic symmetry at long ranges concluded from temperature-dependent neutron diffraction studies [7]. Further, in order to explore the role of atomic ordering at various length scales on MPB-like behavior of KBST5, we have analyzed temperature-dependent Raman scattering and PDF data in the upcoming sections.

4.3.6 Temperature-dependent Raman study of KBST5 ceramics

The intensity of Raman peaks is influenced by the material's intrinsic vibrations and thermal population of phonons. Moreover, the population of phonons increases with temperature [202]. Thus, in order to accurately compare the Raman spectra across different temperatures, the measured Raman intensities are corrected using the Bose-Einstein factor (which accounts for these temperature-dependent effects) given as [262, 263]:

$$I_{\mathrm{C}}(\bar{\nu}) = \frac{I_{\mathrm{m}}(\bar{\nu})}{n(\bar{\nu},T)+1} \tag{4.5}$$

Here, $\mathrm{I_C}(\bar{\nu})$ and $\mathrm{I_m}(\bar{\nu})$ are the Raman intensity calculated after Bose-Einstein correction and the measured Raman intensity, respectively. Moreover, $n(\bar{\nu}, T)$ is described as [262]:

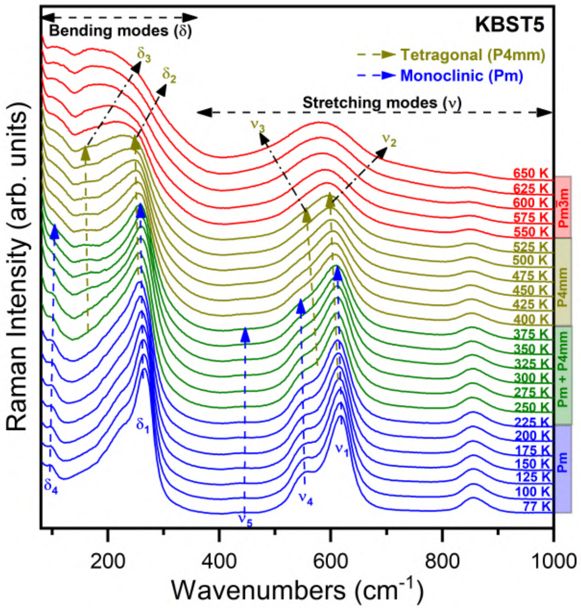

Fig. 4.11 Evolution of temperature-dependent Raman spectra of KBST5 ceramics for 77 K $\leq T \leq$ 650 K.

$$n(\bar{\nu},T) = \frac{1}{exp(\frac{hc\bar{\nu}}{kT}) - 1} \tag{4.6}$$

Here, $\bar{\nu}$, k, and T correspond to wavenumber, Boltzmann constant, and temperature, respectively.

Figure 4.11 depicts temperature-dependent Raman scattering data of KBST5 for 77 K $\leq T \leq$ 650 K. The Raman spectra of KBST5 consist of various Raman active modes, which are classified in two categories *viz.*, stretching (ν) modes or high energy/frequency modes and bending (δ) modes or low energy/frequency modes [20, 21]. Various structural phase transitions *viz.*, monoclinic (Pm) $\rightarrow$ tetragonal ($P4mm$) $\rightarrow$ cubic ($Pm\bar{3}m$), are clearly visible in the Raman spectra (see Fig. 4.11). For $T \geq$ 550 K, no Raman active peaks are visible in the spectra (the peaks flatten), suggesting the presence of a high-temperature cubic phase with $Pm\bar{3}m$ space group (see Fig. 4.11). Here, the cubic phase with $Pm\bar{3}m$ space group exhibits a total of five triply degenerate phonon modes associated with the 1b site, 1a site, and 3d site of the A-site cation, B-site cation, and the oxygen atom, respectively (see Table 4.7) [262]. Out of these five phonon modes, one is an acoustic mode T_{1u}, while the other four are optical modes, comprising three polar T_{1u} modes and one nonpolar T_{2u} mode *i.e.*, $3T_{1u} + T_{2u}$ (see Table 4.7) [262]. Moreover, on lowering temperatures, these triply degenerate phonon modes split into non-degenerate (A_1/B_1) and doubly degenerate (E) phonon modes, resulting in a tetragonal phase (see Table 4.7) stable for $400\ K \leq T \leq 525\ K$, corroborating the inferences drawn from temperature-dependent SXRD data (see Figs. 4.6 and 4.7). The tetragonal phase is described by the presence of various Raman active stretching modes *viz.*, $\nu_2 \approx 610$ cm^{-1} and $\nu_3 \approx 570$ cm^{-1} and bending modes *viz.*, $\delta_2 \approx 250$ cm^{-1} and $\delta_3 \approx 160$ cm^{-1} (see Fig. 4.11). At the lowest measured temperatures *i.e.*, $77\ K \leq T \leq 225\ K$, a monoclinic phase is found to be stable. The monoclinic phase is described by the presence of various Raman active stretching modes *viz.*, $\nu_1 \approx 615$ cm^{-1}, $\nu_4 \approx 550$ cm^{-1} and $\nu_5 \approx 445$ cm^{-1} and bending modes *viz.*, $\delta_1 \approx 260$ cm^{-1} and $\delta_4 \approx 100$ cm^{-1} (see Fig. 4.11). For $225\ K < T < 400\ K$, a co-existence of monoclinic and tetragonal phases is observed in Raman scattering data (see Fig. 4.11). It can be clearly seen from Fig. 4.11 that unique peaks corresponding to tetragonal (ν_3 and δ_3) and monoclinic (ν_4, ν_5, and δ_4) phases co-exist for $225\ K < T < 400\ K$, thereby confirming the morphotropic phase boundary for KBST5.

Further, Fig. 4.12 depicts the evolution of wavenumbers of stretching modes present around 560 cm^{-1} and 605 cm^{-1} as a function of temperature (T). The wavenumbers (or peak positions) of a phonon mode in Raman spectra correspond to the energy of that particular vibrational mode [202]. Various anomalies corresponding to structural phase transitions of KBST5 are clearly visible in the evolution of wavenumbers as a function of temperature (T) (see Fig. 4.12). The first anomaly around 225 K corresponds to the appearance of the tetragonal phase (*P*4*mm*), which is clearly evident from the presence of unique peaks corresponding to stretching (ν_2 and ν_3) and bending modes (δ_2 and δ_3) of tetragonal symmetry (see Fig. 4.11), thereby resulting in to two-phase region (*Pm* + *P*4*mm*) stable up

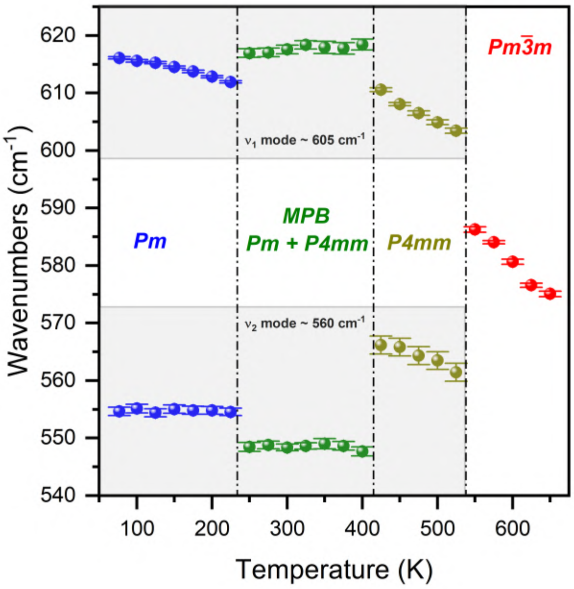

Fig. 4.12 Evolution of wavenumbers of modes around 605 cm^{-1} and 560 cm^{-1} as a function of temperature.

to 400 K. Subsequently, another anomaly near 400 K corresponds to the disappearance of monoclinic phase, thereby resulting again in a single tetragonal phase with *P*4*mm* space group. The exit of monoclinic phase is clearly evident by the disappearance of unique peaks corresponding to stretching (ν_1, ν_4, and ν_5) and bending modes (δ_1 and δ_4) of monoclinic symmetry (see Fig. 4.11). Finally, the last anomaly near 550 K corresponds to the Curie temperature (T_C), which describes the structural phase transition from a ferroelectric phase (tetragonal; *P*4*mm*) to a paraelectric phase (cubic; $Pm\bar{3}m$). Further, the atomic ordering at short ranges will be analyzed using temperature-dependent pair distribution function (PDF) data in the next section.

4.3.7 PDF analysis of KBST5 ceramics at elevated temperatures

The short-range atomic ordering in KBST5 has been determined using temperature-dependent PDF data for a wide temperature range (300 K $\leq T \leq$ 1000 K). The temperature-dependent SXRD analysis confirms various structural phase transitions *viz.*, (*Pm* + *P*4*mm*)

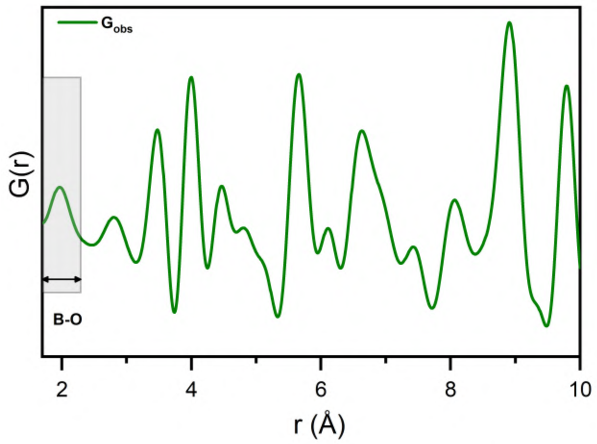

Fig. 4.13 The experimental PDF profile of KBST5 ceramics at 300 K (1.7 Å$\leq r \leq$ 10 Å) .

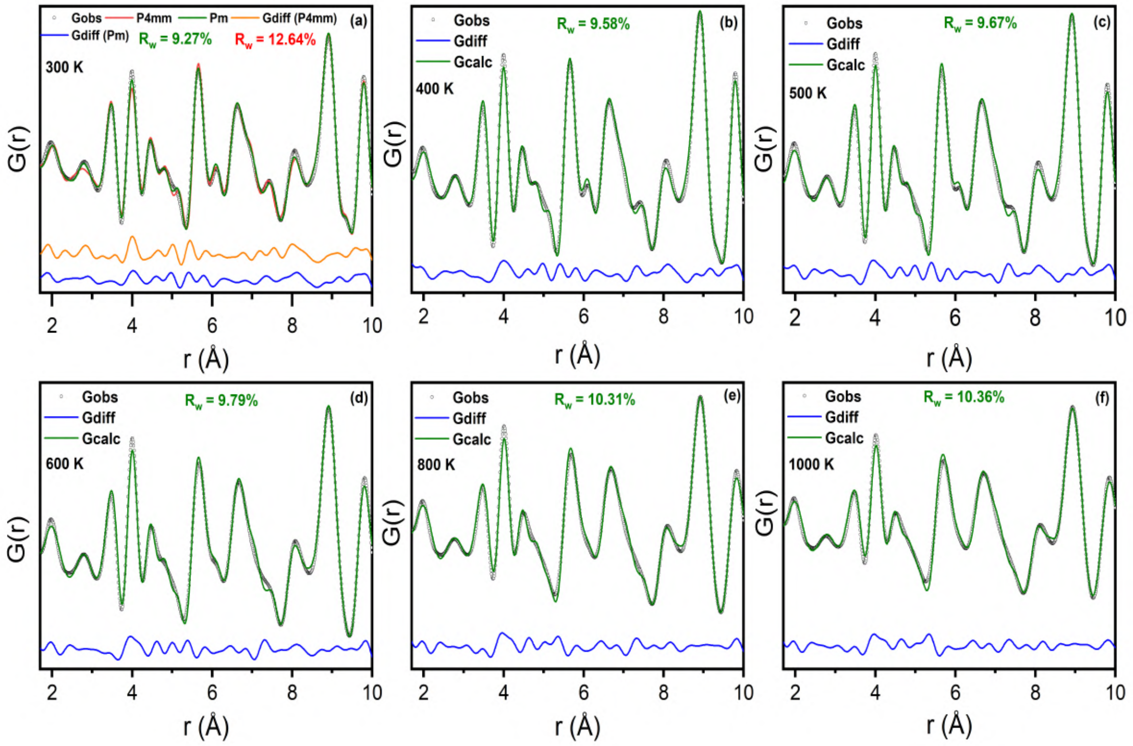

Fig. 4.14 Fitted PDF profiles of KBST5 ceramics as a function of temperature. The open circle, red line, and green line represent observed G(r), fit using the tetragonal model (Space Group: *P*4*mm*), and fit using the monoclinic model (Space Group: *Pm*), respectively. Additionally, the orange and blue lines represent the difference lines between the calculated and observed G(r) pattern for *P*4*mm* and *Pm* models, respectively.

$\xrightarrow{\approx 400K} P4mm \xrightarrow{\approx 550K} Pm\bar{3}m$ at long ranges. The possible atomic ordering at short ranges could be monoclinic (Space Group: *Pm*), tetragonal (Space Group: *P*4*mm*), or cubic

(Space Group: $Pm\bar{3}m$). We have analyzed the PDF data at short ranges for 1.7 Å $\leq r \leq$ 10 Å. For a cubic structure (Space Group: $Pm\bar{3}m$), a single peak corresponding to the first coordination sphere (*i.e.*, B-O × 6 bonds) should be observed. However, the experimental pattern (G_{obs}), clearly demonstrates that the first peak (associated with B-O bond lengths; $r <$ 2.3 Å) results from the convolution of more than one peak (see Fig. 4.13), ruling out the possibility of cubic structure at short ranges. Moreover, in order to test other models in the studied temperature range (300 K $\leq T \leq$ 1000 K), we have fitted the PDF data with monoclinic (Space Group: Pm) and tetragonal (Space Group: $P4mm$) space groups (see Fig. 4.14(a)). It is clearly evident from the fitted profiles and R_w values that the monoclinic model provides a better fit than the tetragonal model at room temperature (see Fig. 4.14(a)), confirming our conclusions inferred from composition-dependent Raman studies and earlier reports from literature [7]. Here, it is important to note that similar behavior has been reported earlier for $NaNbO_3$, where the low-temperature rhombohedral phase stable at long ranges is found to be stable at room temperature for short ranges [27]. Thus, a monoclinic symmetry at short ranges is stable for KBST5 at ambient conditions. Further, this monoclinic symmetry persists up to the highest studied temperature (300 K $\leq T \leq$ 1000 K) (see Figs. 4.14(a)-(f)), similar to what has been observed for KNN50 [56]. On the other hand, the structure at long ranges evolves with temperature as ($Pm + P4mm$) $\xrightarrow{\approx 400K} P4mm \xrightarrow{\approx 550K} Pm\bar{3}m$, suggesting an order-disorder type of transition for KBST5 as a function of temperature (T). This is reminiscent of order disorder-type transition observed for $BaTiO_3$ [264, 265] and KNN50 [56].

Moreover, volume of the monoclinic unit cell at short ranges has also been plotted as a function of temperature (see Fig. 4.15). Two distinct anomalies can be clearly observed at T $\approx$ 400 K and 550 K, consistent with SXRD analysis. The former anomaly corresponds to the disappearance of the monoclinic phase at long-ranges, and has been attributed to the order disorder-type transition temperature above which completely different structures

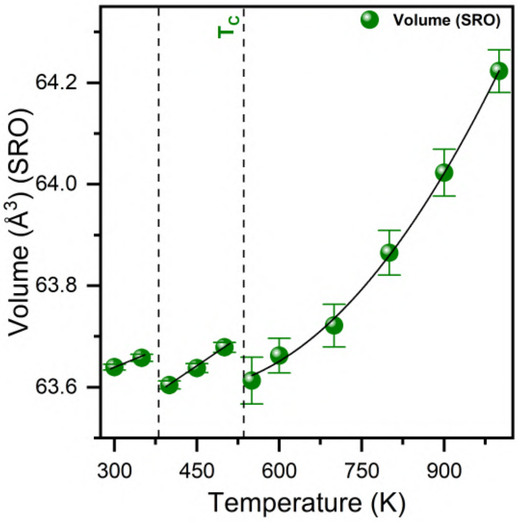

Fig. 4.15 Evolution of volume of KBST5 ceramics at short ranges as a function of temperature.

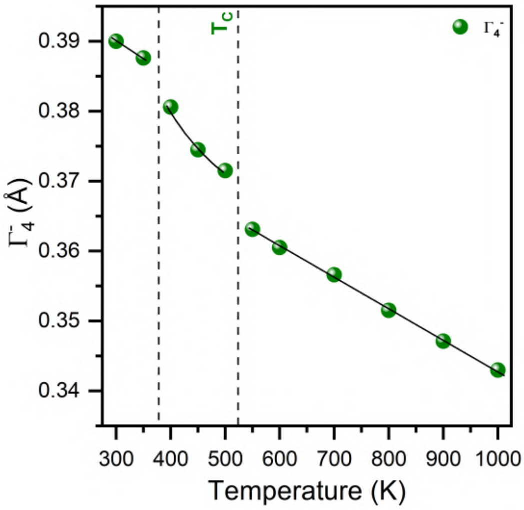

Fig. 4.16 Evolution of the amplitude of ferroelectric phonon mode (Γ_4^-) at short ranges as a function of temperature for KBST5 ceramics.

has been observed at long and short ranges. Another anomaly at T $\approx$ 550 K corresponds to the Curie temperature above which a paraelectric cubic phase is stable at long ranges. Furthermore, the amplitude of the ferroelectric mode (Γ_4^-) has also been calculated for the monoclinic phase using the structural parameters obtained after refining the PDF data. The amplitude of the Γ_4^- phonon mode increases on decreasing temperature, and two anomalies at T ≈ 400 K and 550 K are clearly evident from the plot (see Fig. 4.16). These anomalies are consistent with the characteristic temperatures obtained from SXRD analysis. Thus, combined analysis of X-ray diffraction data, dielectric data, Raman scattering data, and PDF data reveals MPB-like behavior of KBST5 ceramics also linked with order disorder-type transition.

4.4 Conclusion

In conclusion, we have synthesized a Pb-free solid solution of $K_{0.5}Na_{0.5}NbO_3$ (KNN50) with $Ba_{0.9}Sr_{0.1}TiO_3$ (BST10) *viz.*, (1-x)KNN50-xBST10 (KBSTx) for $0.00 \leq x \leq 0.20$ and investigated its long/short-range structures, dielectric properties, and phonon mode crystallography as a function of composition (x) and temperature (T). KBSTx exhibits various structural phase transitions at long ranges along with a two-phase coexistence (monoclinic and tetragonal) and maximum dielectric constant at ambient conditions in the ferroelectric region ($0.00 \leq x < 0.20$) at $x = 0.05$ (KBST5). Moreover, Raman spectra reveal monoclinic symmetry for KBSTx ($0.00 \leq x \leq 0.20$) ceramics. An anomaly in the wavenumber and intensity of ν_2 mode (≈ 550 cm^{-1}) is observed near $x = 0.10$. The integrated analysis of composition-dependent X-ray diffraction and Raman scattering data uncovers a transition from a monoclinic phase at long ranges to a monoclinic phase at short ranges, thereby confirming a transition from an ordered monoclinic structure (Space Group: *Pm*) of KNN50 into a disordered cubic structure (Space Group: $Pm\bar{3}m$) of KBST20. Further, owing to the two-phase coexistence and maximum dielectric constant (in the ferroelectric region) of KBST5, high-temperature Synchrotron X-ray diffraction (SXRD), pair distribution function (PDF), and temperature-dependent Raman scattering data have been used to explore the morphotropic phase boundary (MPB)-like behavior of KBST5. The high-temperature SXRD data demonstrate various structural phase transitions in KBST5 *viz.*, $(Pm + P4mm) \xrightarrow{\approx 400K} P4mm \xrightarrow{\approx 550K} Pm\bar{3}m$. Subsequently, temperature-dependent PDF analysis of KBST5 confirms a monoclinic symmetry at short ranges stable for a wide temperature range (300 K $\leq T \leq$ 1000 K). Moreover, two anomalies are observed at T $\approx$ 400 K and T $\approx$ 550 K in volume and the amplitude of ferroelectric phonon mode (Γ_4^-) obtained from SXRD and PDF analysis. The former anomaly corresponds to an order-disorder type transition, whereas the latter anomaly corresponds to the Curie temperature (T_C). Further, temperature-dependent Raman scattering data of KBST5 demonstrate that the two polar phases *viz.*, monoclinic and tetragonal, co-exist for a wide temperature range (225 K < T < 400 K), suggesting a weak temperature dependence, a feature characterizing MPB-like behavior. Furthermore, the room temperature dielectric constant of KBST5 is found to be more from adjacent compositions *viz.*, KNN50 and KBST10 by 62% and 83%, respectively, and also the amplitude of the ferroelectric phonon mode ($\Gamma_4{}^-$) is maximum for KBST5, thereby confirming MPB-like behavior of KBST5.

In the next chapter, we will explore the temperature-dependent crystal structure of relaxor ferroelectric composition *viz.*, KBST20, and associated physical properties *viz.*, dielectric constant and thermal expansion.